Electronic Supplementary Material (ESI) for Nanoscale.
This journal is © The Royal Society of Chemistry 2024

Supporting Information
A twist for tunable electronic and thermal transport properties of nanodevices

Azar Ostovan,[*,†] Karolina Z. Milowska,[‡] and Carlos J. García-Cervera[*,†]

†*Mathematics Department, University of California, Santa Barbara, CA 93106, USA*

‡*CIC nanoGUNE, Donostia-San Sebastián, Spain*

¶*Ikerbasque, Basque Foundation for Science, Bilbao, Spain*

E-mail: azarostovan@ucsb.edu; cgarcia@ucsb.edu

Note S1: Stability verification calculations

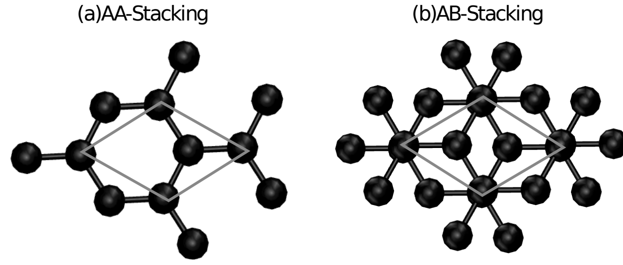

Figure S1: The (a) AA-stacking and (b) AB-stacking patterns of the bilayer graphene.

A comparison of the energy difference between both stacking configurations for the bilayer graphene was made to find out which stacking pattern is more stable in calculations. In good agreement with previous computational study,[1] the AB-stacking of bilayer graphene is more energetically stable, with an energy per atom that is by 0.024 eV/atom below that of the AA-stacking when we use the vdW-DRSLL exchange-correlation potential. However, when we consider the nanodevices constructed from zigzag graphene nanoribbons with a top rectangular benzenoid [6,3]-flake, we find that the AA-nanodevices are more stable than the AB nanodevices, with the AA device having an energy per atom that is lower than that of the AB device by 1.8×10^{-3} eV/atom and 3×10^{-3} eV/atom, when we use the vdW-DRSLL (SIESTA) and PBE-D2 QuantumATK levels of theory, respectively.

Note S2: Energy band gaps

Table S1: Energy band gaps (E_g) of the analyzed AA-devices calculated using DFT with the PBE-D2 exchange-correlation functional.

Device	E_g (eV)
AA-1.1°	0.0398
AA-2.2°	0.0351
AA-4.4°	0.0276
AA-6.6°	0.0110
AA-8.8°	0.0000

As shown in Table S1, the size of the energy band gap can be controlled by varying the twisting angle between the nanoribbon and the flake. E_g decreases with increasing θ value and closes at θ=8.8°.

Note S3: Band structure calculations of central part of the AA nanodevice

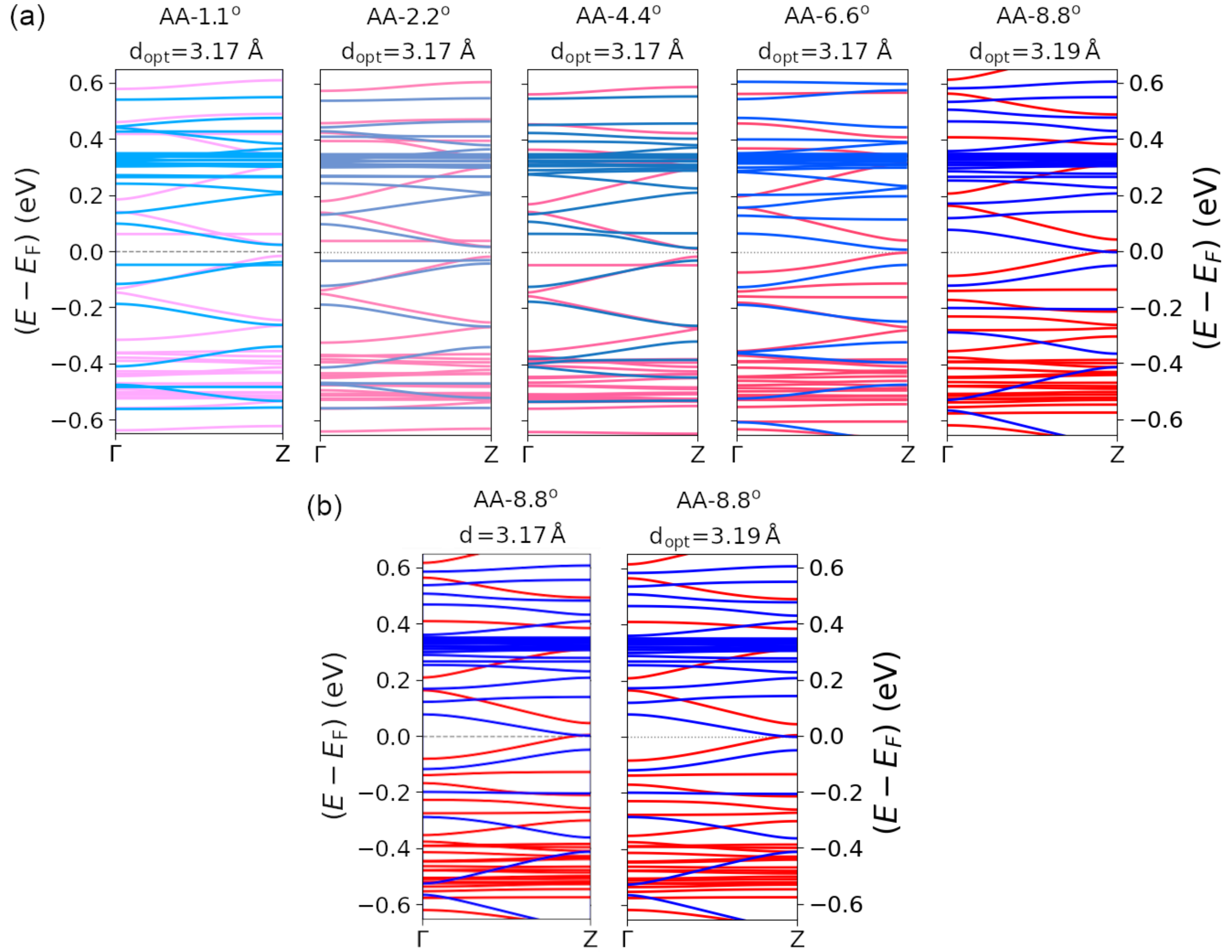

Figure S2: (a) Evolution of the electronic band structure of the central parts of all studied AA nanodevices as a function of the twisting angle, θ. (b) Comparison between bands structures of AA-8.8^o system at different distances between the flake and the nanorribon. Results were obtained in ATK code using DFT/PBE-D2 level of theory.

To verify whether varying twisting angle, θ, changes the optimal distance between the flake and the nanoribbon, we performed similar calculations to the calculations described in the method part. For each AA system (central part of the device with 3D periodic boundary conditions applied; bulk configuration), we placed the flake at different distances and calculated the total energies. The optimal distances between the flake and the nanoribbon at which the total energy of each system is the lowest (d$_{opt}$) are the same for all our AA nanodevices, except for AA-8.8. The optimal distance is equal to 3.17 for AA-0.0^o, AA-1.1^o,

AA-2.2^o, AA-4.4^o and AA-6.6^o systems, whereas, for AA-8.8^o system, d_{opt} is equal to 3.19 . In Fig. S2 (a) we plotted the band structures for each AA system at the optimal distance, while in panel (b) we show the band structures of AA-88° at d=3.17 and d_{opt}=3.19 . The observed difference in the band structures in panel b is very small and does not change the conclusion. The band gap is closed. For AA-88° system, we observe the band crossing at the Fermi level that is slightly more pronounced for d_{opt} than it is for d=3.17 .

Note S4: Difference in spin population on the edges on the flake

Table S2: Difference in spin population between major and minor spin components ($Q_{\uparrow} - Q_{\downarrow}$) of the top flake in AA-devices calculated using DFT with vdW-DRSLL exchange-correlation functional.

Device	$Q_{\uparrow} - Q_{\downarrow}$
AA-1.1°	-0.05
AA-2.2°	-0.66
AA-4.4°	-0.85
AA-6.6°	+1.20
AA-8.8°	-0.12

The difference in spin population between major and minor spin components ($Q_{\uparrow} - Q_{\downarrow}$) of the top flake may change as it twists. For AA devices, the values of $Q_{\uparrow} - Q_{\downarrow}$ are listed in Table S2. It seems that with twisting, the difference in spin population increases until AA-6.6° and then reduces. Another point is that the sign of $Q_{\uparrow} - Q_{\downarrow}$ has changed for AA-6.6°. The overall result is that during twisting, the nanoflake edges remain spin-polarized, and the difference in edge spin polarization increases with the increasing of twisting, then reduces for AA-8.8°.

Note S5: Local device density of states analysis

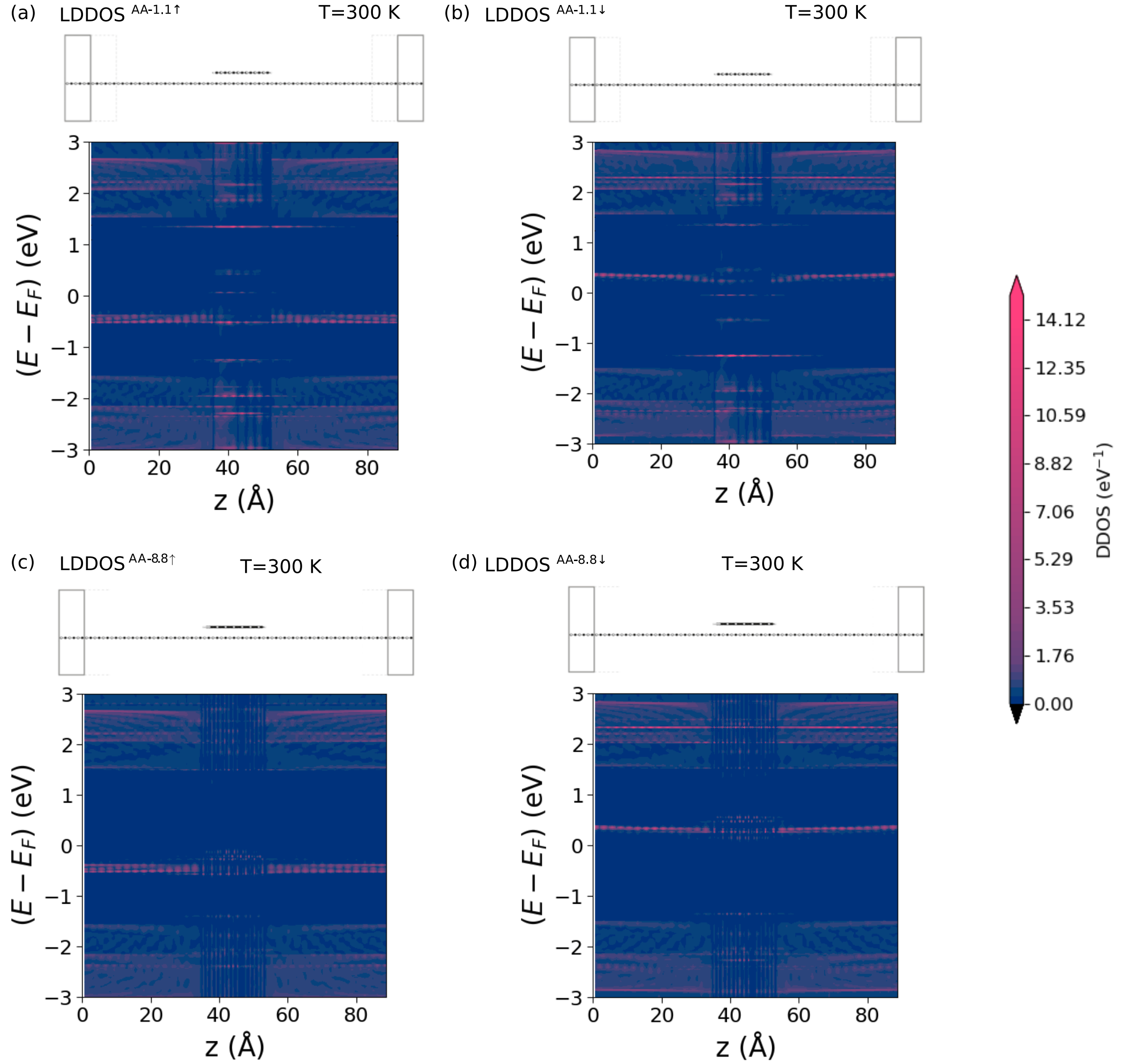

Figure S3: The calculated spin-polarized local device density of states (LDDOS) of (a) AA-$1.1^{\uparrow}$ and (b) AA-$1.1^{\downarrow}$ at T = 300 K; (d) AA-$8.8^{\uparrow}$ and (e) AA-$8.8^{\downarrow}$ at T = 300 K using the PBE-D2 level of theory. The side views of system considered are shown above each LDDOS map.

As we discussed in the main text, reducing the device symmetry through twisting for AA-nanodevices results in an inbalance between the spin components electronic inverse participation ratio (see Figure 1, main text). Local device density of states (LDDOS) analysis (Figure S3) shows that for AA-1.1 nanodevices these edge states are more localized over the

bottom ZGNR layer (Figure S3(a)-(b)) and, via twisting, states which are localized over the top [6,3] rectangular flake also appear at energies close to those of the bottom layer (Figure S3(c)-(d)).

Note S6: Electronic Inverse Participation Ratio (IPR)

The IPR for a system of N atoms can be defined as:[2]

$$IPR = \Sigma_{i=1}^{N} |q_i^{(n)}|^2, \tag{1}$$

$$q_i^{(n)} = \Sigma_{\mu\epsilon i,\nu} \mathrm{Re}[S_{\mu\nu} c_{\mu n}^{*} c_{\nu n}], \tag{2}$$

where S is the overlap matrix and $c_{\mu n}$ are the coefficients of the n-th wavefunction in the LCAO basis. The inverse participation ratio is $1/N$ for completely delocalized states and greater for localized states.

Note S7: Transmission spectra plots for different twisting angles.

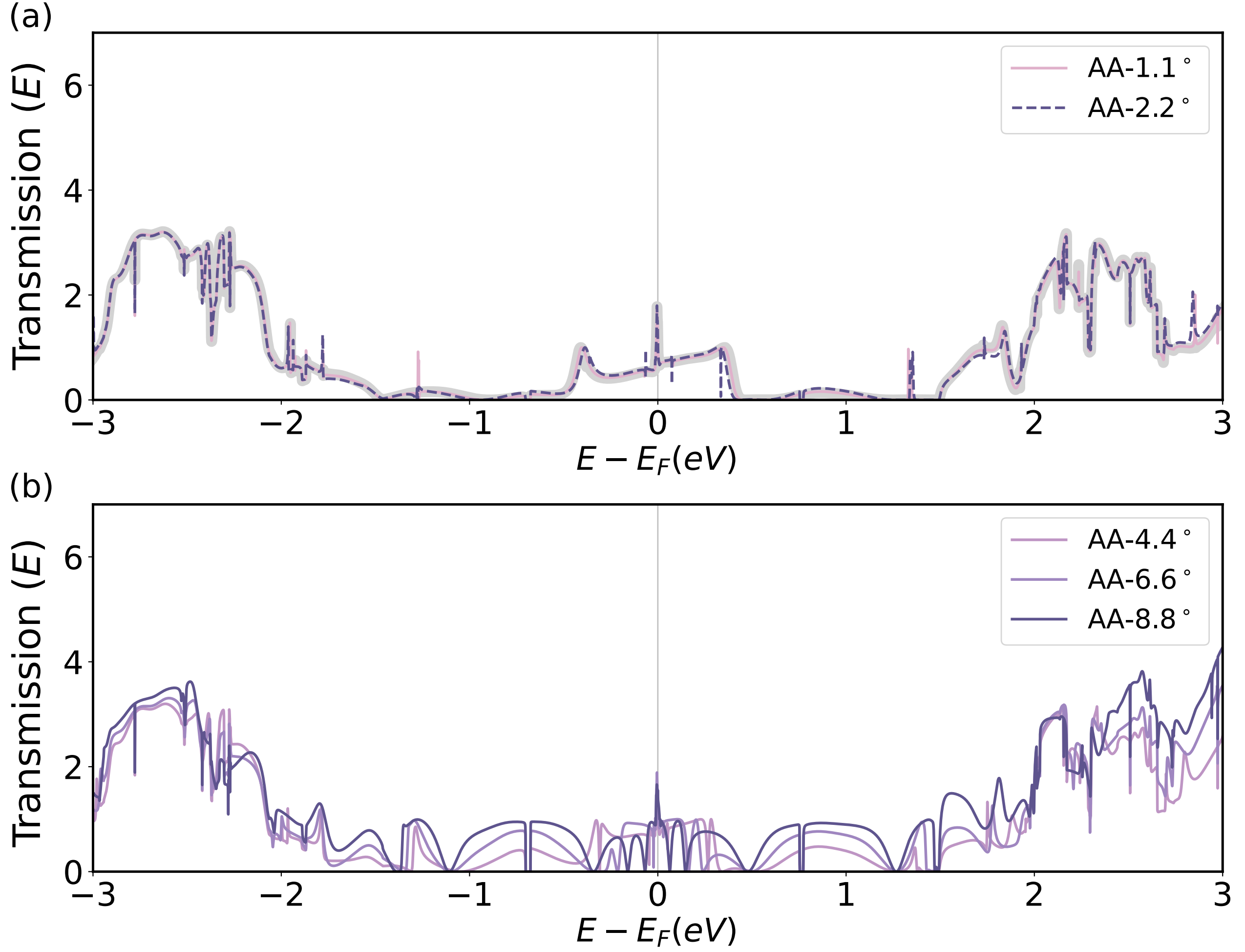

Figure S4: Plot of the average transmission coefficients over energy levels as a function of energy ($E - E_{\mathrm{F}}$) for different twisting angles (θ) using the vdW-DRSLL level of theory. (a) Transmission spectra of AA-0.0° $\leq \theta \leq$ AA-4.4° and (b) Transmission plot of AA-6.6° $\leq \theta$ $\leq$ AA-8.8°.

As the transmission spectra of the AA-stacking devices show (Figure S11(b)), the transmission values present an angular dependency and gradually increase as the top flake is rotated from θ= 4.4° to 8.8°. The variation is more pronounced at energies around $\pm$ 1 $\leq E$ $\leq \pm$ 0.5. The transmission values remain almost unchanged in the lower twisting devices, θ $<$ 4.4° (Figure S11(a)).

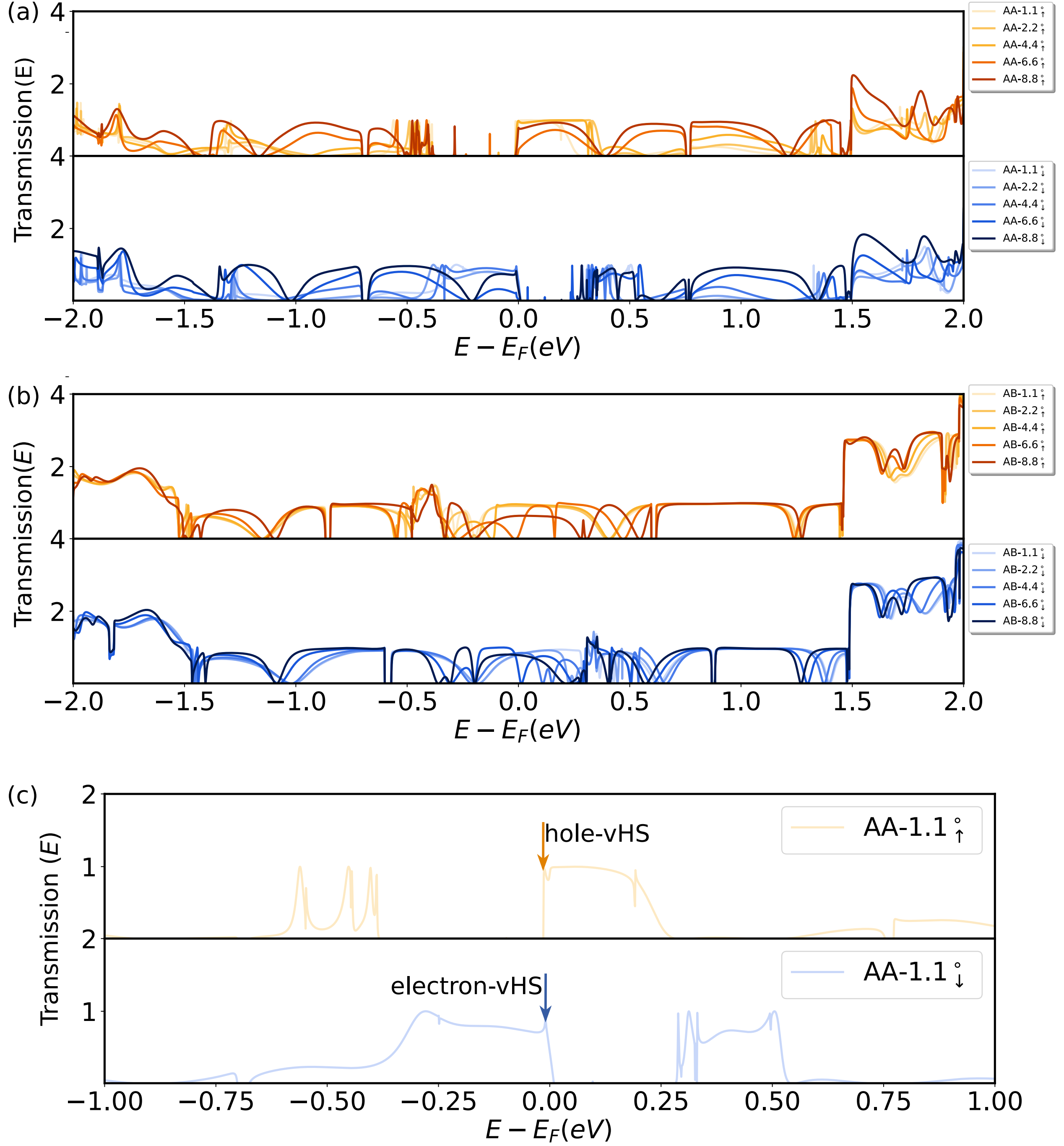

Figure S5: Spin-resolved average transmission coefficients over energy levels spectra of (a) AA-devices and (b) AB-devices as a function of energy ($E - E_\mathrm{F}$) for different twisting angles (θ) using the vdW-DRSLL level of theory.(c) The energetic positions of electron and hole-vHSs in transmission spectra of AA-1.11.1° using the vdW-DRSLL exchange-corrolation functional which is indicated by dark orange and dark blue arrows.

The plot of spin-resolved transmission (Figure S5(a)) for AA-devices reveals the polar-

ization of the transmission at energies close to E_{F}, while this feature was not observed in the AB-devices (Figure S5(b)). Based on this behavior we computed the current−voltage characteristic for AA-1.1° and AA-8.8° nanodevices (Figure 2(e), main text) which shows the level of polarization especially at negative voltages. Figure S5(c) shows the signature of electron and hole-van Hove singularities in spin-polarized transmission spectra of AA-1.1° devices.

Note S8: Transmission eigenstates analysis

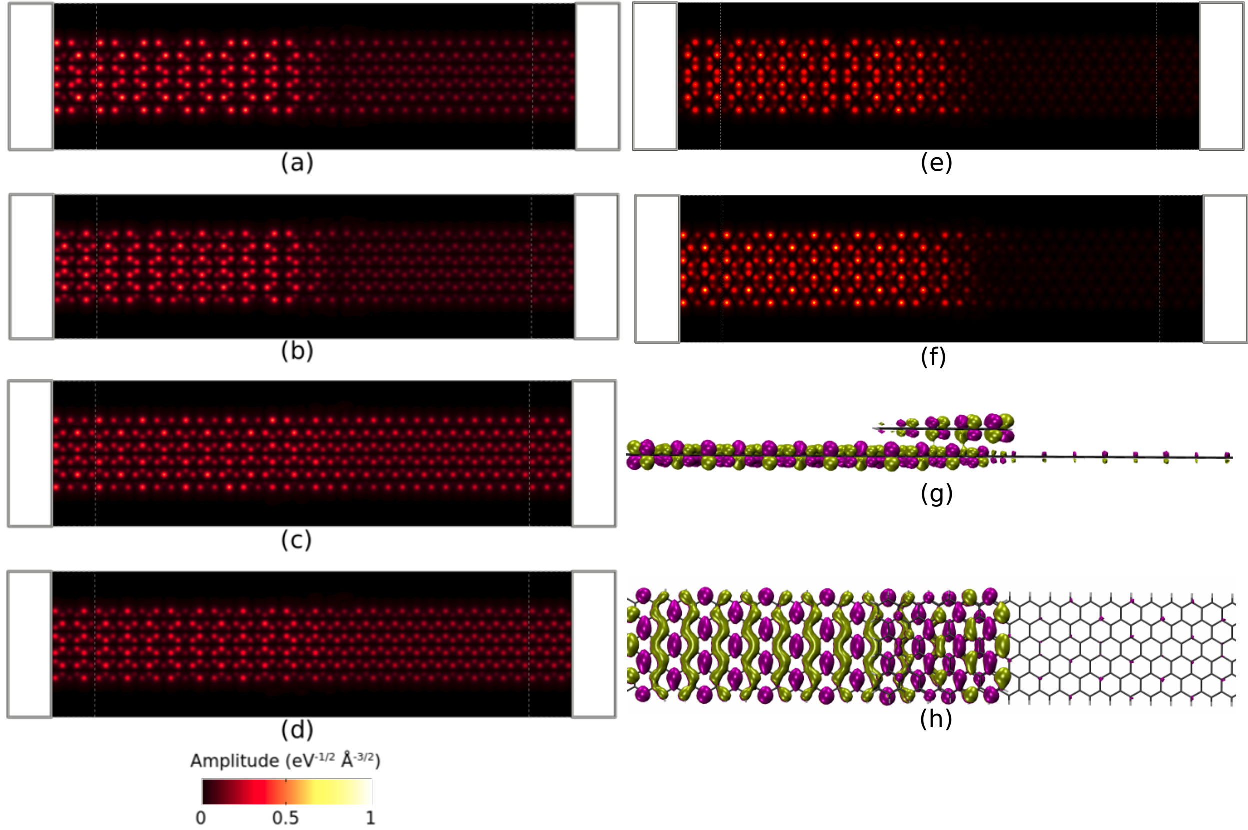

Figure S6: Spin-resolved transmission eigenstates for the bottom layer of (a) AA-1.1$^{\circ}_{\uparrow}$, (b) AA-1.1$^{\circ}_{\downarrow}$, (c) AB-1.1$^{\circ}_{\uparrow}$, (d) AB-1.1$^{\circ}_{\downarrow}$ junctions at $E = -0.8$ eV and (e) AA-1.1$^{\circ}_{\uparrow}$, (f) AA-1.1$^{\circ}_{\downarrow}$ at $E = -0.8$ eV using the PBE-D2 level of theory. The molecular-projected self-consistent Hamiltonian (MPSH) of (g) top and (h) side view of AA-1.1° nanodevices at $E = +0.8$ eV. The MPSH plots are obtained using DFT/vdW-DRSLL level of theory.

Spin-dependent eigenstate analysis (Figure S6 (SI)) shows the localization of conductance states over the central region and right side of the low-twisted AA-devices (AA-1.1$^{\circ}_{\uparrow}$ and AA-1.1$^{\circ}_{\downarrow}$ in Figure S6(a)-(b)). In such devices the $\mathbf{p}_z$ orbitals of the top flake and bottom layer form strong hybridization which leads to electron transport from the bottom layer to the top GNR flake. Consequently, electrons are trapped on the top flake and cannot contribute to the current conductance. For AA devices with higher twisting angles $4.4^{\circ} \leq \theta \leq 8.8^{\circ}$ and AB-devices (AB-1.1$^{\circ}_{\uparrow}$, and AB-1.1$^{\circ}_{\downarrow}$ in Figure S6(c)-(d)) there is no effective hybridization between the central twisted layers, and electrons can easily flow from the first to the second

electrode. In these devices, the eigenstates are distributed over the whole length of the device. The transmission eigenstates for $E = +0.8$ eV (Figure S6(e)-(f)) appear to be similar to those for $E = -0.8$ eV, as discussed above.

Note S9: Temperature dependence of electrical conductance for different doping levels

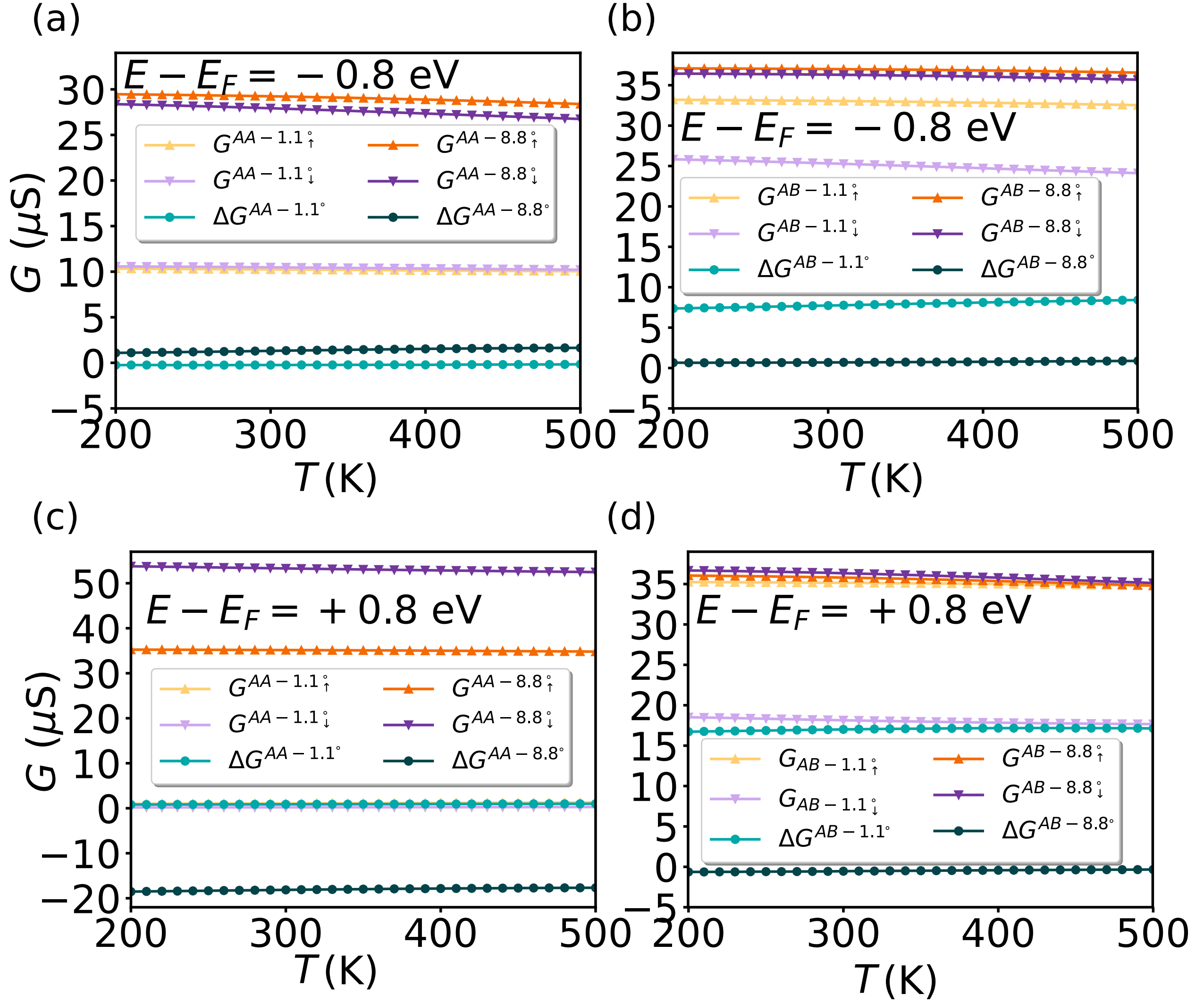

Figure S7: Spin-resolved electrical conductance (G) of (a) AA-1.1° and AA-8.8° at $E = -0.8$ eV, (b) AB-1.1° and AB-8.8° at $E = -0.8$ eV, (c) AA-1.1° and AA-8.8° at $E = +0.8$, (d) AB-1.1° and AB-8.8° at $E = +0.8$ eV as a function temperature (T) using PBE-D2 level of theory.

Figure S7 shows the variation of conductance vs temperature for two specific energies at which the largest variation in G was obtained as a result of twisting. We can see the doping level can somehow influence the electrical conductance in different temperatures for both stacking configurations.

Note S10: Temperature dependence of Seebeck's coefficient for different doping levels

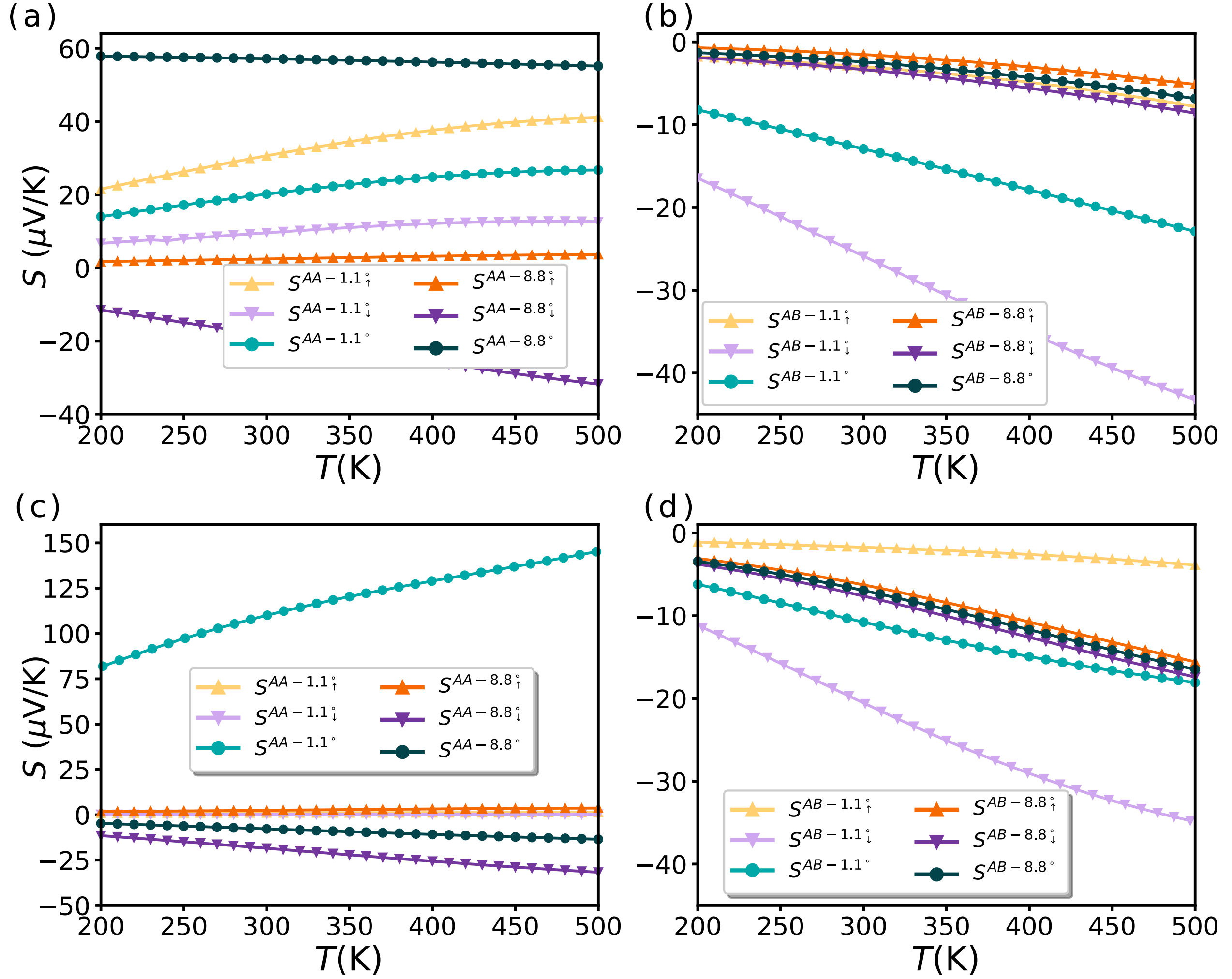

Figure S8: Spin-resolved Seebeck coefficient (S) of (a) AA-1.1° and AA-8.8° at $E = -0.8$ eV, (b) AB-1.1° and AB-8.8° at $E = -0.8$ eV, (c) AA-1.1° and AA-8.8° at $E = +0.8$ eV and (d) AB-1.1° and AB-8.8° at $E = +0.8$ eV, as a function of temperature (T) using PBE-D2 level of theory.

The positive and negative values of S reflect the contribution of both hole and electron in heat transport through the devices. Regardless of the type of heat carrier in the systems, the S and so on the thermopower efficiency increases with rising temperature. The thermopower efficiency is affected by the twisting angle at the studied electrochemical potentials (Figure S8) though it does not show a distinct dependency as what was observed at the Fermi level

for AA-twsitronic (Figure 4(a) and 4(b), main text).

Note S11: Temperature dependence of thermal conductance for different doping levels

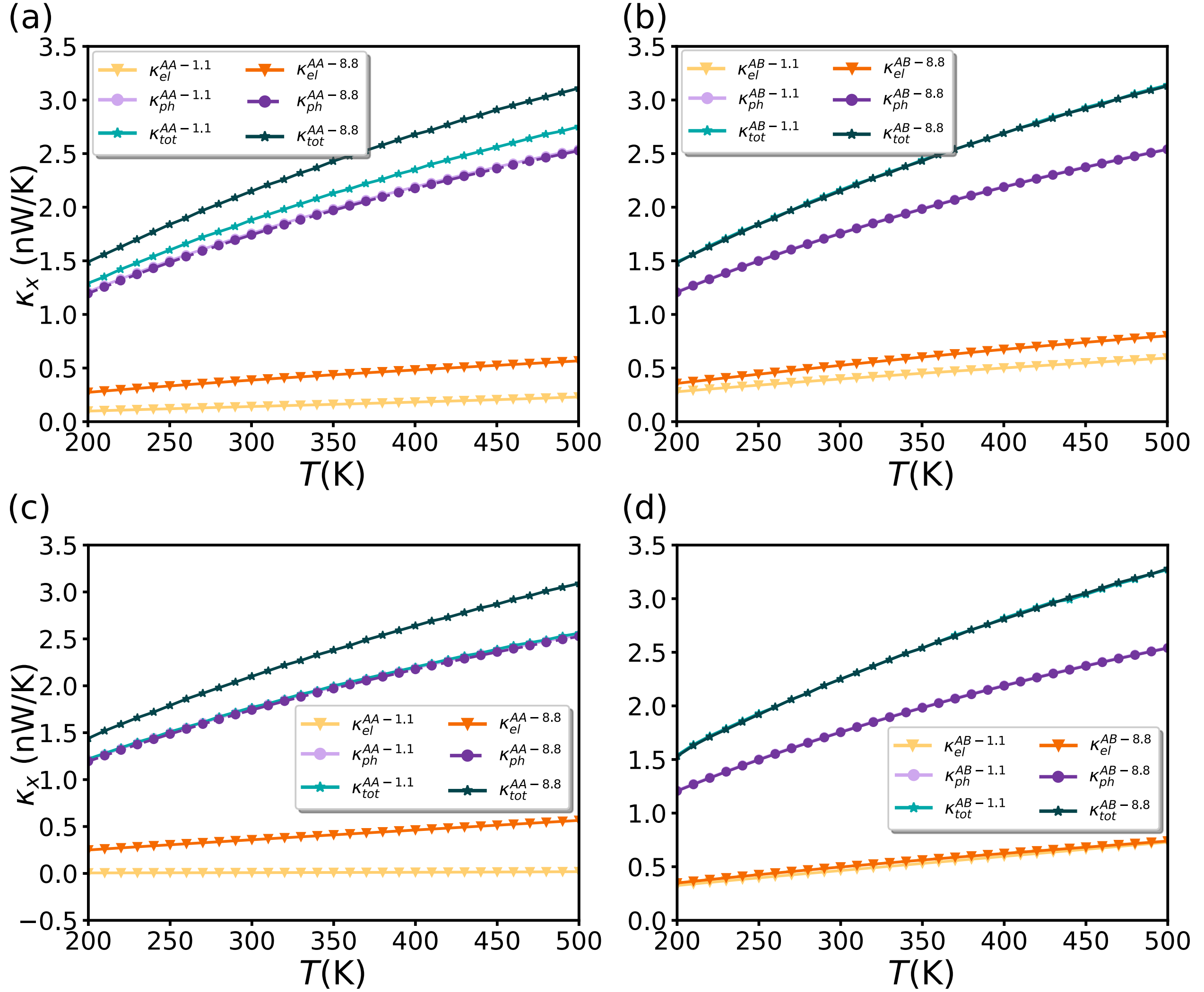

Figure S9: Electron (κ_e), phonon (κ_{ph}) , and total thermal conductivity (κ_{tot}) of (a) AA-1.1° and AA-8.8°, (b) AB-1.1° and AB-8.8° at $E = -0.8$ eV; (c) AA-1.1° and AA-8.8° (d) AB-1.1° and AB-8.8° at $E = +0.8$ eV.

The total value of κ smoothly increases by T for AA and AB devices at both electrochemical potentials (Figure S9).

Note S12: Electrode structure

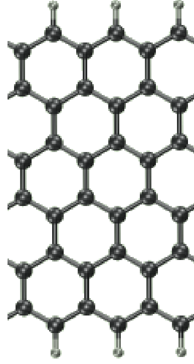

Figure S10: Structure of 6-ZGNR electrodes used for device simulations.

Electrodes are composed of three relaxed 6-ZGNR unit cells. Both electrodes are attached to 6–ZGNR bottom layer. After geometry relaxation, we conducted a scan of the lattice parameter along the periodic direction to identify the value at which the electrode cell exhibits the lowest energy. Based on conducted simulations, the lattice parameter along the periodic direction (c) has a value of 7.43 Å. The lattice distance in the transverse direction (a and b) is set at 25 Å to mitigate spurious electrostatic interactions. This method has been successfully employed in previous studies involving graphene[3] and metallic electrodes.[4]

Note S13: Computational approaches in device simulations

As Van der Waals (vdW) force functionals are not still implemented in QuantumATK, we have chosen the exchange-correlation functional PBE-D2 to account for vdW interactions in QuantumATK simulations. We show in Figure S1 a comparison between the conductance values for AA-1.1° computed using TranSIESTA and QuantumATK. Although the results show significant quantitative differences, they do share some qualitative similarities. In addition, one can see that, except for energy values around the Fermi level, E_F, the values of Transmission computed using Dion, Rydberg, Schröder, Langreth, and Lundqvist (DRSLL), which is implemented in TranSIESTA, are a lower value, but in good correspondence with the results computed using the PBE-D2 exchange-correlation functional, which is implemented in QuantumATK. The calculated transmission using the DRSLL approach is higher by the value of 0.3 G_0 at the Fermi level.

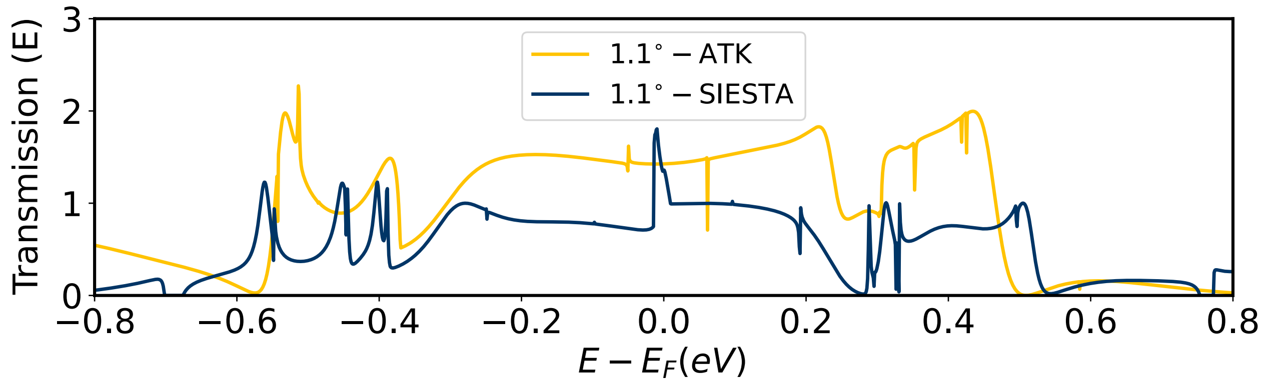

Figure S11: Comparison between the simulated values of the average transmission coefficients over energy levels as a function of electrochemical potential ($E - E_\mathrm{F}$) for the AA-1.1° device using PBE-D2 exchange-correlation functional which is implemented in QuantumATK (orange curve) and DRSLL exchange-correlation functional which is implemented in SIESTA code (blue curve).

Note S14: Details of the thermoelectric simulations

The thermoelectric calculations were performed with the QuantumATK numerical package[5–7] using the DFT/PBE-D2/DZ level of theory for the electronic contribution and a reactive force field[8] for the phonon component. In this approach, the Landauer - Büttiker formula[9] for the electronic current through the device under a finite bias voltage, U, can be expressed as the sum of two terms:

$$I = \Delta\mu \frac{2q}{h} \int_{-\infty}^{\infty} \overline{T}(E,U) \frac{\partial f(E,\mu,T)}{\partial \mu} \mathrm{d}E + \Delta T \frac{2q}{h} \int_{-\infty}^{\infty} \overline{T}(E,U) \frac{\partial f(E,\mu,T)}{\partial T} \mathrm{d}E, \tag{3}$$

where ΔT and $\Delta\mu$ are small changes to the temperature of the electrode temperature, T, and to the electrochemical potential μ, respectively. $\overline{T}(E)$ is the energy-resolved transmission function and $f(E,\mu,T)$ is the Fermi-Dirac electron distribution function.

Similarly, the electron thermal current in this device can be expressed as:

$$I_Q = \Delta\mu \frac{2q}{h} \int_{-\infty}^{\infty} \overline{T}(E,U)(E-\mu) \frac{\partial f(E,\mu,T)}{\partial \mu} \mathrm{d}E + \Delta T \frac{2q}{h} \int_{-\infty}^{\infty} \overline{T}(E,U)(E-\mu) \frac{\partial f(E,\mu,T)}{\partial T} \mathrm{d}E. \tag{4}$$

Hence, the electrical conductance G, the Seebeck coefficient S and the electron thermal conductance κ_e can be expressed as:

$$G = \left. \frac{dI}{dU} \right|_{dT=0} = q^2 L_0, \tag{5}$$

$$S = -\left. \frac{dU}{dT} \right|_{I=0} = \frac{1}{qT} \times \frac{L_1}{L_0}, \tag{6}$$

$$\kappa_e = \left. \frac{dI_Q}{dT} \right|_{I=0} = \frac{1}{T} \times \left(L_2 - \frac{L_1^2}{L_0} \right), \tag{7}$$

where

$$L_n(\mu,T) = \frac{2}{h} \int G(E)(E-\mu)^n \left[-\frac{\partial f(E,\mu,T)}{\partial E} \right] \mathrm{d}E. \tag{8}$$

Note that the total Seebeck coefficient of a spin-polarized system is not the simple sum of spin-dependent Seebeck coefficients:[10]

$$S = \frac{G_\uparrow S_\uparrow + G_\downarrow S_\downarrow}{G_\uparrow + G_\downarrow}, \tag{9}$$

where $G_\uparrow$ and $G_\downarrow$ are spin dependent conductances and $S_\uparrow$ and $S_\downarrow$ are the spin-dependent Seebeck coefficients.

The phonon thermal conductance was calculated based on the Landau formula:[9,11]

$$\kappa_{ph} = \frac{1}{2\pi} \int \overline{T}_{ph}(\omega)\omega\hbar \left[-\frac{\partial n(\omega, T)}{\partial T} \right] \mathrm{d}\omega, \tag{10}$$

where $\overline{T}_{ph}(\omega)$ is the frequency-resolved phonon transmission function, n is the Bose-Einstein phonon distribution function and T is the temperature of the electrode.

The total thermal conductance, κ, was calculated as a sum of electron (κ_e) and phonon (κ_{ph}) thermal conductances.

References

S1. Birowska, M.; Milowska, K.; Majewski, J. Van der Waals Density Functionals for Graphene Layers and Graphite. *Acta Phys. Pol.* **2011**, *120*, 845–848.

S2. Simdyankin, S.; Elliott, S.; Hajnal, Z.; Niehaus, T. A.; Frauenheim, T. Simulation of Physical Properties of the Chalcogenide Glass As_2S_3 Using a Density-Functional-Based Tight-Binding Method. *Phys. Rev. B* **2004**, *69*, 144202.

S3. Ostovan, A.; Mahdavifar, Z.; Bamdad, M. Length–dependence of conductance in benzothiadiazole molecular wires between graphene nanoribbon electrodes: Effect of conformational changes. *J. Mol. Liq.* **2018**, *269*, 639–649.

S4. Ostovan, A.; Papior, N.; Naghavi, S. S. Half-metallic porphyrin-based molecular junctions for spintronic applications. *Phys. Rev. B* **2021**, *104*, 235435.

S5. Synopsys QuantumATK Version 2022.03-SP1 (accessed 11-07-2023). `https://www.synopsys.com/silicon/quantumatk.html`.

S6. Stokbro, K.; Petersen, D.; Smidstrup, S.; Blom, A.; Ipsen, M.; Kaasbjerg, K. QuantumATK: An Integrated Platform of Electronic and Atomic-Scale Modeling Tools. *J. Condens. Matter Phys.* **2020**, *32*, 015901.

S7. Stokbro, K.; Petersen, D.; Smidstrup, S.; Blom, A.; Ipsen, M.; Kaasbjerg, K. Semiempirical Model for Nanoscale Device Simulations. *Phys. Rev. B* **2010**, *82*, 075420.

S8. Mao, Q.; Ren, Y.; Luo, K.; van Duin, A. C. D. Dynamics and Kinetics of Reversible Homomolecular Dimerization of Polycyclic Aromatic Hydrocarbons. *J. Chem. Phys.* **2017**, *147*, 244305.

S9. Datta, S. *Electronic Transport in Mesoscopic Systems*; Cambridge University Press, 1997.

S10. Ashcroft, N. W.; Mermin, N. D. *Solid State Physics*; New York: Saunders College Publishing, 1976.

S11. Jiang, J.-W.; Wang, J.-S.; Li, B. A Nonequilibrium Green's Function Study of Thermoelectric Properties in Single-Walled Carbon Nanotubes. *J. Appl. Phys.* **2011**, *109*, 014326.